BIOLOGICAL SCIENCES: Developmental Biology

Intercellular calcium waves are controlled by morphogen signaling during organ development

Qinfeng Wu[1,*], Pavel A. Brodskiy[1,*], Cody Narciso[1], Megan Levis[1], Jianxu Chen[2], Peixian Liang[2], Ninfamaria Arredondo-Walsh[1], Danny Z. Chen[2], and Jeremiah J. Zartman[1,#]

[1]Department of Chemical and Biomolecular Engineering, University of Notre Dame, 205D McCourtney Hall, Notre Dame, IN 46556, USA
[2]Department of Computer Science and Engineering, University of Notre Dame, 326E Cushing Hall, Notre Dame, IN 46556, USA

*These authors contributed equally to this work

[#]Email for correspondence: jzartman@nd.edu
[#]Phone number for correspondence: 574-631-0455

Key words: Quantitative biology; pattern formation; signal transduction; dynamic systems; reverse engineering; developmental biology; image analysis

Abstract

Spontaneous and dramatic intercellular calcium waves are frequently observed during organ development, but are poorly understood. Calcium ions are ubiquitous second messengers that carry out a wide-range of functions, including the regulation of cell proliferation, metabolism and death. Consequently, regulation of calcium signaling encodes a significant portion of the cellular decision making state of cells through both amplitude and frequency-dependent regulation of transcription factors and key regulatory enzymes. Here we report that intercellular calcium waves exhibit spatiotemporal patterns at the organ-level using a quantitative image analysis pipeline. Intercellular calcium waves in the *Drosophila* wing disc require a specific phospholipase C, Plc21C. Further, we demonstrate that the morphogen signaling pathway, Hedgehog, controls frequencies of calcium oscillations uniformly in the tissue and is required for non-uniform spatial patterning of oscillation amplitudes. Thus, the dynamics of spontaneous intercellular calcium waves are regulated by morphogenetic signaling. Intercellular calcium waves propagate information at the organ-scale that reflects the differentiation state of the developing wing disc.

Significance Statement

Both calcium signaling and the Hedgehog pathway are essential in directing tissue and organ development in many organisms. This paper reports the first observation that the Hedgehog pathway, which patterns the anterior-posterior orientation of many tissues, spatially patterns intercellular calcium waves in the developing limb of fruit flies. Using image analysis, we show that calcium wave amplitude is higher in the posterior of the tissue, that wave activity decreases during development, and that perturbing the Hedgehog pathway abolishes the amplitude patterning and uniformly changes the frequency. Consequently, morphogenetic signaling results in a secondary level of pattern formation that emerges in calcium waves. Understanding how calcium dynamics encode morphogenetic information at the tissue scale will provide insights into development and cancer.

Introduction

Calcium (Ca^{2+}) is a ubiquitous second messenger that is a central player in cellular differentiation, proliferation, wound healing and regeneration (4–10). Ca^{2+} signals are usually oscillatory and can encode information through several features, including peak amplitudes, frequencies, widths of oscillations, and basal cytoplasmic concentrations, which are then selectively decoded by downstream effector molecules that include regulatory enzymes and transcription factors (11–13). Thus, Ca^{2+} signals can compactly convey a large set of information on the cellular regulatory state. Spontaneous intercellular Ca^{2+} waves (ICWs) occur in many tissue types. For example, ICWs are involved in ensuring robust wound healing and regeneration (7, 9, 14) and have been observed in multicellular developmental contexts such as butterfly pupal wings (15) and in *Drosophila* larval wing discs (9, 16, 17). However, how ICWs emerge or how they are controlled at the organ scale is largely unknown. Understanding the regulation of ICWs in organs will provide insights into development (1–3, 18), as well as diseases such as Alzheimer's disease (19) and metastatic cancers (20).

Organ development relies on precise, long-range communication of information among cells. During development, spatial information is conveyed by the concentration of morphogen molecules that specify cell fates (21–24). For example, Hedgehog (Hh) is an important morphogen that directs anterior-posterior (A/P) cell identity in tissues of most animals with bilateral symmetry (25). Hh signaling is also essential for specifying the A/P patterning in the *Drosophila* wing disc, which develops into the wing of the adult fly and has led to many discoveries defining mechanisms of organ development (25–27). Hh signaling has two

2

mechanistic branches: 1) slower, canonical signaling, through regulation of the transcription factor *cubitus interruptus (ci)*, and 2) fast, noncanonical signaling, through the protein $G\alpha_i$ (28). A recent study has shown that noncanonical Hh signaling regulates spikes of Ca^{2+} in frog neural tubes (29), but the spatiotemporal regulation of intercellular Ca^{2+} signaling by Hh and other morphogens is unknown.

Results

Characterizing ICWs in wing discs

Recent results from both our group (14, 30, 31) and others (9, 16) have reported gap-junction based intercellular Ca^{2+} transients in the wing imaginal disc. ICWs can be imaged in wing discs with the genetically encoded calcium indicator GCaMP6f sensor to visualize relative concentrations of cytoplasmic Ca^{2+} (Fig. 1*A*) (32). Spontaneous ICWs are robustly observed using an *in vivo* imaging setup to characterize ICW activity in the wing disc pouch (Fig. 1*B*). We observed spontaneous ICWs in 35% of larva imaged over a twenty-minute period (n = 25/72), in qualitative agreement with a recent study (9) (Fig. 1*D, D'*, Movie S1). However, *in vivo* imaging provides limited information due to larval motion, mechanical compression, and an inability to specifically perturb the organ with drugs (33–35). Therefore, we cultured discs *ex vivo* to enable higher resolution imaging (Fig. 1*C*). We initially used the chemically-defined ZB media, which supports culture of wing disc-derived Clone 8 cells for over 100 passages as a starting point to identify possible chemical signals impacting ICW activity (30). Discs cultured in ZB media without fly extract did not yield ICWs (Fig. 1*E, E'*, Movie S2). We found that supplementation of ZB media with fly extract (30), which is serum produced from ground flies, was required to observe ICWs *ex situ* in wing discs (Fig. 1*F, F'*, Movie S3). Therefore, fly extract is necessary and sufficient to produce ICWs, in agreement with the suggestion that specific signals in fly extract are required to stimulate ICWs (16, 30).

Stimulation of ICWs requires the PLCβ1 homolog Plc21C.

To quantify ICW dynamics, we developed an image analysis algorithm to extract Ca^{2+} signatures from each disc (Fig. 2*A-B*, Fig. S1-3) and combined them into multi-disc composites (Fig. 2*C*, Fig. S1-3). The algorithm calculates the relative amplitudes, which represent the average increase in intensity of the signal relative to basal intensity; frequencies, which represent the numbers of events over time; width at half max, which represents the length of time that the Ca^{2+} signal is active; and basal intensity levels, which reflect the basal Ca^{2+} concentration of a cell (Fig. 2*B*). The spatial distributions of these summary statistics were measured (Fig. 2*C*), transformed onto "average" axes (Fig. 2*D*), and composited (Fig. 2*E*, Fig. S1-3).

To elucidate the mechanism behind fly extract-induced ICWs, we used RNA interference (RNAi) to systematically knock down components of the Ca^{2+} signaling pathway (Fig. 2*F*) and measured changes in ICW dynamics. Phospholipase C (PLC) catalyzes the production of inositol-1,4,5-triphosphate (IP_3), which binds to and stimulates IP_3 receptor (IP_3R) on the endoplasmic reticulum (ER) to release Ca^{2+} from the ER (Fig. 2*D*). However, the isoform of PLC responsible for stimulating ICWs is unknown. We tested all PLC homologs in *Drosophila* for a Ca^{2+} wave phenotype. We found that expression of $Plc21C^{RNAi}$ (PLCβ1 homolog), completely extinguishes ICW activity in the wing disc (Fig 2*G*, Movie S4). Knockdown of the other PLC homologs—PLCγ homolog *small wings* (*sl*) and PLCβ4 homolog *norpA*—did not affect ICWs (Fig. 2*G*, Movie S5, S6). Additionally, we confirmed several of the components previously implicated in Ca^{2+} signaling in the wing disc are required for ICW dynamics through RNAi experiments: ICWs require Ca^{2+} release through IP_3R, Ca^{2+} recycle through SERCA and diffusion through gap junctions (9, 14, 16, 30, 36) (Movie S7-9). Ca^{2+} channels Stim, Orai and PMCA did not qualitatively impact ICWs activity (Movie S10-12).

3

Spatial patterning of ICW signatures emerges throughout development

During observation of experiments, we noted a striking difference in Ca^{2+} intensity between the anterior (A) and posterior (P) compartments of wing discs (Fig.1A, 2), suggesting spatial patterning of Ca^{2+} signals. For all discs imaged, 77% of discs had higher average amplitudes (Amp) in the P compartment. The average Amp is approximately 39% higher in the P compartment than the A compartment (Fig 3A, Table S1). To further investigate spatiotemporal patterning of Ca^{2+} signatures, we examined spatial distributions of Ca^{2+} signatures in pouches of different developmental ages. To do so, we grouped the wing discs by pouch size, which can be used to approximate the developmental age of a larva (37) (Fig. 3, Table S1). We found that the difference in amplitudes between compartments increases with increasing pouch size (Fig. 3A, B, Table S1). The frequency was independent of pouch size (for linear or exponential fit, adjusted $R^2 < 1 \times 10^{-3}$, Fig. 3A, C). The width at half max is weakly correlated with pouch size, and was not spatially patterned between compartments in the pouch (Fig. 3A, D). Basal intensity decreases with increasing pouch size (Fig. 3A, E). Averaged over the compartment level, frequencies are only slightly different (paired t-test, $p > 0.3$ for Class I, $p < 0.05$ for Class II), which likely indicates that frequency is driven primarily by diffusion, while the driving force behind amplitude is the difference between Ca^{2+} concentration in the cytoplasm and ER of individual cells (Fig. 3A, C). These results show that the overall basal level decreases as the discs mature and that a spatial patterning of ICW amplitudes across the A-P axis emerges at later stages of development. The spatial patterning of ICW activity during wing disc growth suggests that ICWs convey long-distance spatial information to cells, in effect providing a memory of morphogenetic spatial information throughout the tissue (38).

Canonical Hh signaling modulates ICW frequency and directs amplitude patterning

The discovery of A/P patterning of average ICW amplitudes led us to suspect the involvement of Hh signaling, which directs the development of the A and P compartment boundary (39–41). Hh signaling activity is dependent on the protein Smoothened (Smo), whose activity is inhibited by the receptor Patched (Ptc) (27). Smo binds to the Hedgehog Signaling Complex (HSC) containing the protein Costal2 (Cos2), the kinase Fused (Fu) and the transcriptional factor Cubitus interruptus (Ci) (27). In the absence of Hh, HSC controls the cleavage of full length Ci (Ci155) to a truncated repressor form, Ci^R (27). Suppressor of Fused (SuFu) retain Ci155 in the cytoplasm to oppose its nuclear import (42). Binding of Hh to Ptc blocks Ptc-mediated Smo inhibition, allowing Smo to signal to reduce Ci cleavage (27). Noncanonical Hh signaling is the result of the activation of $G\alpha_i$ by Smo (28). $G\alpha_i$ has many downstream effects including reducing the concentration of cyclic AMP (cAMP), which in turn inhibits Protein Kinase A (PKA) (28).

To determine the effect of canonical Hh signaling on ICWs, we analyzed ICWs in genetically perturbed wing discs. To determine whether Hh signaling is responsible for spatial patterning of ICW amplitudes, we examined the spatial pattern of average Amp in the A and P compartments for all previously mentioned conditions (Fig. 4A). The knockdowns were validated by examination of the wing phenotypes (Fig. S4, Table S2). Expression of full-length Ci (UAS-*ci*) resulted in deformed wing pouches with no intracellular waves and little Ca^{2+} activity. We grouped different genetic perturbations into canonical activation (UAS-*ci*$^{PKA-}$, UAS-*ci*, UAS-*fu*), canonical suppression (UAS-*smo*^{RNAi}, UAS-*cos2*, UAS-*ci*^{RNAi}) and combined canonical and noncanonical activation (UAS-*smo*^{CA}) based on their corresponding functions and wing phenotypes (Fig. S4). For example, the overexpression of Cos2 is known to downregulate canonical Hh signaling by blocking Smo accumulation, while expression of Fu is known to rescue this phenotype (43). We found that canonical suppression was sufficient to abolish spatial patterning of ICW amplitudes between the A and P compartments (Fig. 4B, C). However,

4

acute drug perturbations and canonical activation did not alter the spatial pattern of ICW amplitudes (Fig. 4*B, C*, all p>0.05).

In addition, we analyzed the change of ICW frequencies under different perturbations. Canonical Hh activators tended to have lower average frequencies in the pouch than the control (control: 1.7 ± 0.8 mHz, UAS-*ci*: 0.6 ± 0.5 mHz, p<0.02, and UAS-*ci*$^{PKA-}$: 1.1 ± 0.5 mHz, p<0.005, Fig. 4*D, E*, Movie S13-15, Table S3), and all three canonical Hh suppressors tended to have higher average frequencies than the control (UAS-*smo*^{RNAi}: 3.3 ± 0.6 mHz, p<4x10^{-6}, UAS-*cos2*: 2.1 ± 0.6, p<0.08, and UAS-*ci*^{RNAi}, 1.8 ± 0.4 mHz, p<2x10^{-4}, Fig. 4*D, E*, Movie S16-18, Table S3). Suppression of Smo increased average Ca^{2+} oscillation frequencies *in vivo*, where ICWs occurred twice as frequently in the *smo*^{RNAi} condition relative to the tester line (Fig. 5*A*, Movie S19). These results demonstrate that Smo controls ICW frequencies by a canonical mechanism. However, activation of Smo through *smo*^{CA} led to a multimodal distribution of average ICW frequencies in the pouch, including normal, higher ICW frequency, or severe reduction of ICWs (Movie S20). The heterogeneous *smo*^{CA} data is consistent with an interpretation that *smo*^{CA} also activates ICWs through both canonical and noncanonical mechanisms.

To investigate the possibility of noncanonical activation of ICW frequency, we used a variety of drugs to acutely perturb the noncanonical Hh pathway and the downstream PKA pathway. Cyclopamine serves as an antagonists to canonical Hh signaling, but agonists to Smo-based noncanonical signaling (44), which is the only signaling mechanism that can impact Ca^{2+} signaling on the timescale of the experiment (<2 hr of incubation and imaging) (45). SQ 22536 suppresses cAMP, a downstream target of noncanonical Hh signaling, through adenylyl cyclase inhibition. All three drugs tended to increase the ICW frequency relative to a 0.1% DMSO control (DMSO: 1.3 ± 0.9 mHz, Cyclopamine: 2.5 ± 0.8 mHz, p<0.02, SQ 22536: 2.7 ± 0.4 mHz, p<7x10^{-3}, Fig. 4*D, E*, Movie S21-24, Table S3). Together with the canonical results, this indicates that modulation of ICW frequencies by Hh follows a paradoxical signaling motif (46, 47), wherein Hh signaling activity leads to reduced ICW frequency through canonical signaling and increased ICW frequency through the noncanonical signaling branch (Fig. 5*B*).

Overall, these results indicate that Hh is required for amplitude patterning of ICWs through a mechanism that requires canonical signaling, which is not affected by acute drug perturbations. In this study, we did not explore long-term drug experiments out of a concern of possible artifacts that might arise from long-term *ex vivo* incubations.

Discussion

Here, we report the discovery that spontaneous ICW activity during wing disc development is regulated by morphogenetic signaling. Quantitative analysis reveals A/P patterning of average ICW amplitudes and temporally decreasing basal intensity as wing discs reach their terminal size before pupariation. We have also demonstrated that Hh signaling is necessary for spatial patterning of ICW amplitude, and that Hh signaling modulates ICW frequency, through canonical decreases and noncanonical increases of frequency. We focused on the 3rd instar discs based on the availability of the nub-Gal4 driver which is active during this stage of development.

Since the stimulation of ICWs in *ex vivo* culture depends on fly extract, it will be important to elucidate the active components in fly extract that stimulate ICWs. Our result indicates that ICWs specifically and selectively require *Plc21C* (*PLCβ1*), and inhibition of either *sl* or *norpA* has no effect on ICW activity. Therefore, *Plc21C* can be modulated to selectively regulate ICWs in future studies. The A/P patterning of ICW amplitudes suggests a potential biological function of ICWs in conveying or storing spatial information in wing discs. One possible mechanism to be

5

tested in the future is that Hh signaling regulates ICWs through Plc21C activity, which may be a direct regulatory target of Ci, as the *Plc21C* enhancer has Ci binding sites, and is responsive to Hh signaling (48). Further, canonical Hh signaling has many target genes, including the Decapentaplegic and Wingless pathways. Future studies will investigate the interplay between Ca^{2+} and other morphogen pathways to test morphogenetic signaling downstream of Hh may mediate the regulation of ICW dynamics. Preliminary results, however, indicate that ICW activity is also sensitive to perturbations in these pathways.

Another explanation for the patterning of ICWs is that Hh regulates ICWs patterning through actomyosin-mediated mechanical stress. Hh pathway regulates tissue bending, folding and invagination through regulating actomyosin in *Drosophila* eye discs (49), embryo (50) and fore-gut (51). Narciso et al. showed that ICWs can be stimulated by the release of compression in wing discs (30). They have also shown that laser ablation, which leads to rapid dissipation of mechanical stress, leads to Ca^{2+} flashes in the wing discs cultured in FEX-free media (17). In addition, recently it was shown that the myosin II inhibitor blebbistatin interrupted Ca^{2+} oscillations in the wing disc (16). Taken together, Hh signaling may regulate ICW patterning by differential regulation of actomyosin in different compartments. Alternatively, differential ICW activity may reflect difference in growth dynamics and metabolic activities between the two compartments (52). ICWs could then be a phenotypic response to growth and represent stress dissipation that occurs as the tissue size increases.

Our results demonstrate that Hh signaling modulates ICW frequency through an incoherent feed-forward loop (I-FFL, Fig. 4h) (53). An I-FFL is a feed-forward loop with two arms of opposite function. I-FFLs characteristically function as pulse-generators and response accelerators (53–55). This suggests that Ca^{2+} frequency responds to changes in Hh signaling rapidly. Additionally, chronic suppression of both legs of the I-FFL through *smo*^RNAi expression resulted in an increase in frequency (Fig. 4), suggesting that canonical Hh suppression has a greater effect on the frequency than noncanonical Hh activation. Uncovering the role of Ca^{2+} as an integrator of morphogenetic signaling integration in the wing disc will yield insights into the function of similar roles of crosstalk between morphogen and Ca^{2+} signaling pathways in other systems. Intriguingly, the spatial patterning of ICW amplitudes hints at additional spatial patterning roles during wing disc development. Combined with evidence that ICWs and gap junction communication facilitate wound healing (9, 56), this evidence demonstrates that ICWs may be a component of the posited 'memory' system required for pattern repair during tissue regeneration (38). Similar to the use of ECG measurements to understand brain activity, Ca^{2+} waves in epithelial development offer an integrated readout of many cellular processes. Image analysis pipelines that elucidate how specific features of Ca^{2+} signaling correspond to cell signaling state within the tissue context also will be useful in drug development, tissue engineering, and regenerative medicine applications (57).

Materials and Methods
Fly strains and genetics
Gene perturbations to the core Ca^{2+} and Hedgehog signaling pathways (UAS-*Gene X*^RNAi or UAS-*Gene X* (overexpression) were crossed to a genetic tester line (*nub-GAL4, UAS-GCaMP6f/CyO*) that enables combined visualization of Ca^{2+} signaling with down regulation of genes through expression of RNAi in the wing disc. When possible, multiple independent RNAi lines were tested for each gene investigated (Table S2, 4). Stocks are obtained from Bloomington *Drosophila* Stock Center as indicated by stock number (BL#). Progeny wing phenotypes are from F1 male progeny emerging from the nub-Gal4, UAS-GCaMP6f/CyO x UAS-X cross and shown in Fig. S5. The tester line (w1118; nubbin-GAL4, UAS-GCaMP6f/CyO) was generated by recombining P{UAS-Dcr-2.D}1, w1118; P{GawB}nubbin-AC-62 (BL#25754)

6

with w1118; P{20XUAS-IVS-GCaMP6f}attP40 (BL#42747). Flies were raised at 25°C and 12 hour light cycle.

In vivo imaging setup

Wandering 3rd instar *nub-GAL4*, *UAS-GCaMP6f/CyO* larvae were collected for imaging and rinsed vigorously in deionized water. They were dried completely and then adhered to a coverslip for imaging with scotch tape covering the larvae. The larvae were attached with their spiracles facing toward the coverslip to insure the wing discs were aligned toward the microscope. An EVOS Auto microscope was used to image the larvae. The larvae were imaged at 20x magnification for 20 minutes; images were taken every 15 seconds.

Organ culture media

ZB media + 15% fly extract contains 79.4% (v/v) ZB media, 0.6% insulin, 15% ZB-based fly extract and 5% penicillin/streptomycin (33). ZB media was developed as a chemically defined media to support *Drosophila* cell culture(34), and was used as the basal media for most experiments. ZB-based fly extract is undefined serum extracted from ground flies using ZB media as the base. It is commonly used in culture media as a substitute of fetal bovine serum (FBS) to support *Drosophila* tissue growth and prolong the culture time of cultured wing discs. ZB-based fly extract is made from the following protocol: One gram well-nourished mature flies, were homogenized in a tissue homogenizer (15 ml capacity, 0-1 mm clearance) with 6.82x ml of ZB media. This homogenate was centrifuged at 2600 rpm for 20 min at 4°C. The supernatant and the oily film above it were removed and heat-treated at 60°C for 20 min. This preparation was then spun at 2600 rpm for 90 min at 4°C. The supernatant (fly extract) was removed, sterilized by 0.2 μm filters, and stored at 4°C.

Wing disc imaging setup

Wing discs were dissected from 3rd instar larvae and cultured and imaged in the organ culture media on a cover slip based on our previously developed protocol (33). A cell culture insert (EDM Millipore), after truncated the legs, was put on top of the pool of media to immobilize the wing discs. 50 μL of embryo oil was added along the outer periphery of the insert to seal. 100 μL of *organ culture* media was added on top of membrane of the insert. The setup was then transferred to a confocal microscope for Ca^{2+} activity imaging. Imaging was performed on a Nikon Eclipse T*i* confocal microscope (Nikon Instruments, Melville, NY) with a Yokogawa spinning disc and MicroPoint laser ablation system (Andor Technology, South Windsor, CT). Image data were collected on an iXonEM+ cooled CCD camera (Andor Technology, South Windsor, CT) using MetaMorph® v7.7.9 software (Molecular Devices, Sunnyvale, CA). All experiments were performed immediately following dissection to minimize time in culture, except for drug experiments that were incubated for one hour in drug solution or vehicle carrier control prior to imaging. Discs were imaged at a three z-planes with a step size of 10 μm, 20x magnification and 10-second intervals for a total period of one hour, with 200 ms exposure time and 44% to 70% laser intensity. Image intensity was linearly normalized to be comparable at 50% laser intensity.

Data pre-processing

Microscopy resulted in 4D time-lapse data (512 pixels by 512 pixels by 3 z-planes by 361 time points). The z-stack data was max-projected in FIJI (58) to yield z-projected time-lapse videos. Discs that moved over the imaging session by more than several cell diameters were registered with the *StackReg* function in FIJI. Time points were selected such that discs were only analyzed during times in which discs were immobile, with the shortest time-lapse analyzed being 20 minutes (Fig. S1).

For each disc, an ROI defining the pouch was manually selected in MATLAB, and a binary mask was generated. A Gaussian filter was applied to the mask to smooth the polygon into a disk shape. The major axis orientation was calculated for the mask, and the video was rotated such that the major axis was horizontal. The posterior (P) and dorsal (D) compartments were identified manually based on the characteristic shapes of the posterior and anterior compartments (Fig. S3). Pouches were flipped such that the A compartment was on the left, and the D compartment was on the top.

Feature extraction
For each pouch sample, between 803 and 6,083 signals were obtained by taking average intensity (F(t)) from 4x4 pixel (2.8 µm x 2.8 µm) spatial bins arrayed with square packing across the segment disc pouch (Fig. S1A). Video durations ranged from 20 to 60 minutes (Fig. S1B-C). Each signal was decomposed into the following features: amplitude, frequency, width at half max, and basal intensity, which comprise the Ca^{2+} signature of the ROI. Amplitude (Amp) is defined as the mean of the amplitudes of the peaks, where the amplitude of each peak is the prominence of the peak in the *findpeaks* algorithm. Frequency (F, mHz) is the number of peaks detected divided by the length of the signal in time. The width at half max (WHM, s) is defined as the time that a peak is above the peak value minus half the prominence. The basal intensity (B, arbitrary units) represents the equilibrium cytoplasmic concentration of Ca^{2+}, and is the minimum of the signal (Fig. 2, Fig. S1D-E).

To reduce stochastic noise, the normalized intensity ($\Delta F(t)/F_o$) was approximated by using a bandpass Gaussian filter. Spikes in signaling activity were extracted from $\Delta F(t)/F_0$ using the MATLAB *findpeaks* algorithm, with a minimum amplitude (Amp_{min}), refractory period, and width at half max (WHM_{min}), for a total of five parameters. MATLAB's genetic algorithm *ga* was used to calibrate the feature extraction parameters (Fig. 2, Fig. S3, Table S4). To generate reference values, 233 signals (I(t)) were randomly selected from the 656,000 total signals, and manually annotated to identify the times (t_1 and t_2) at which each peak begins and ends. From this, the basal level was taken to be:

$$B_{manual} = \min\big(I(t\epsilon[t_1, t_2])\big)$$

the amplitude was extracted, as equal to:

$$Amp_{manual} = \max\big(I(t\epsilon[t_1, t_2])\big) - B_{manual}$$

and the width at half max (WHM) was taken to be:

$$\text{WHM}_{manual} = \text{sum}\left(I(t\epsilon[t_1, t_2]) > \frac{(Amp_{manual} - B_{manual})}{t_2 - t_1}\right)$$

The genetic algorithm was run at default settings for 172 generations. The objective function Err_1 was the sum of the squared differences of the correlation coefficients of the manual measurements and automatic measurements normalized to manual measurements. Err_2 was the fraction of signals with no waves incorrectly selected to contain waves compared to the manual ground-truth annotated data:

$$Err_1 = \sqrt{\left(\frac{Amp_{manual} - Amp_{auto}}{Amp_{manual}}\right)^2 + \left(\frac{WHM_{manual} - WHM_{auto}}{WHM_{manual}}\right)^2 + \left(\frac{B_{manual} - B_{auto}}{B_{manual}}\right)^2}$$

8

$$Err_2 = \frac{1}{N}\sum_i^N (WHM_{manual} = 0 \text{ \& } WHM_{auto} > 0)$$

where N is the number of signals analyzed (N = 233). A pareto front was generated to demonstrate the trade-offs between summary statistic error and false positives, and parameter values were selected (Fig. S2, Table S5).

Statistical Analysis

The median of ROIs in each disc for each summary statistics was compared across genetic conditions, pouch sizes, and between compartments (Fig. 2, Fig. S3). ROIs within two spatial bins of the edge were excluded from the median, because several occasions would briefly drift out of frame. To compare across conditions, the two-tailed, unpaired, Student's t-test was performed. Significance was verified with the Wilcoxon rank sum test, which gave similar results (Table S3). To compare across compartments, medians were taken after dividing discs into A compartment and P compartment such that the boundary was a vertical line fitted to points along the A/P axis as described in (Fig. S3). The two-tailed, paired Student's t-test was performed. Significance was verified with the Wilcoxon signed-rank test, which gave similar results. (Table S1). The F-test for model fit relative to a constant model was used to determine whether each summary statistic was related to pouch size (Fig. 3).
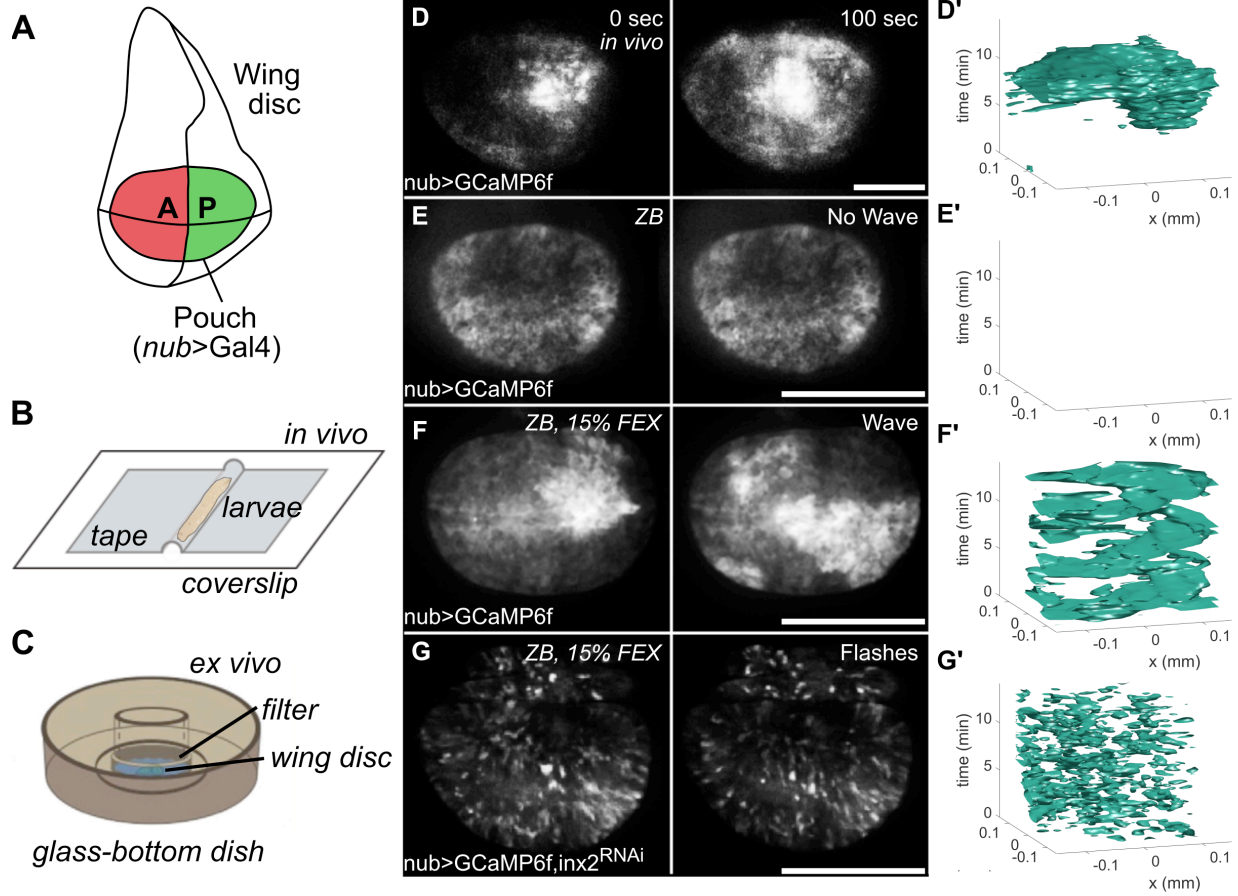
Visualization

To explore the impact of spatial position, developmental progression, and genetic/drug perturbations on Ca^{2+} signatures, we represented each disc as a spatial map, and obtained a spatial composite map for each condition. These spatial composites were mapped to a canonical representation (defined by the average pouch) based on the coordinate system transformation proposed in (Fig. S6) (59).
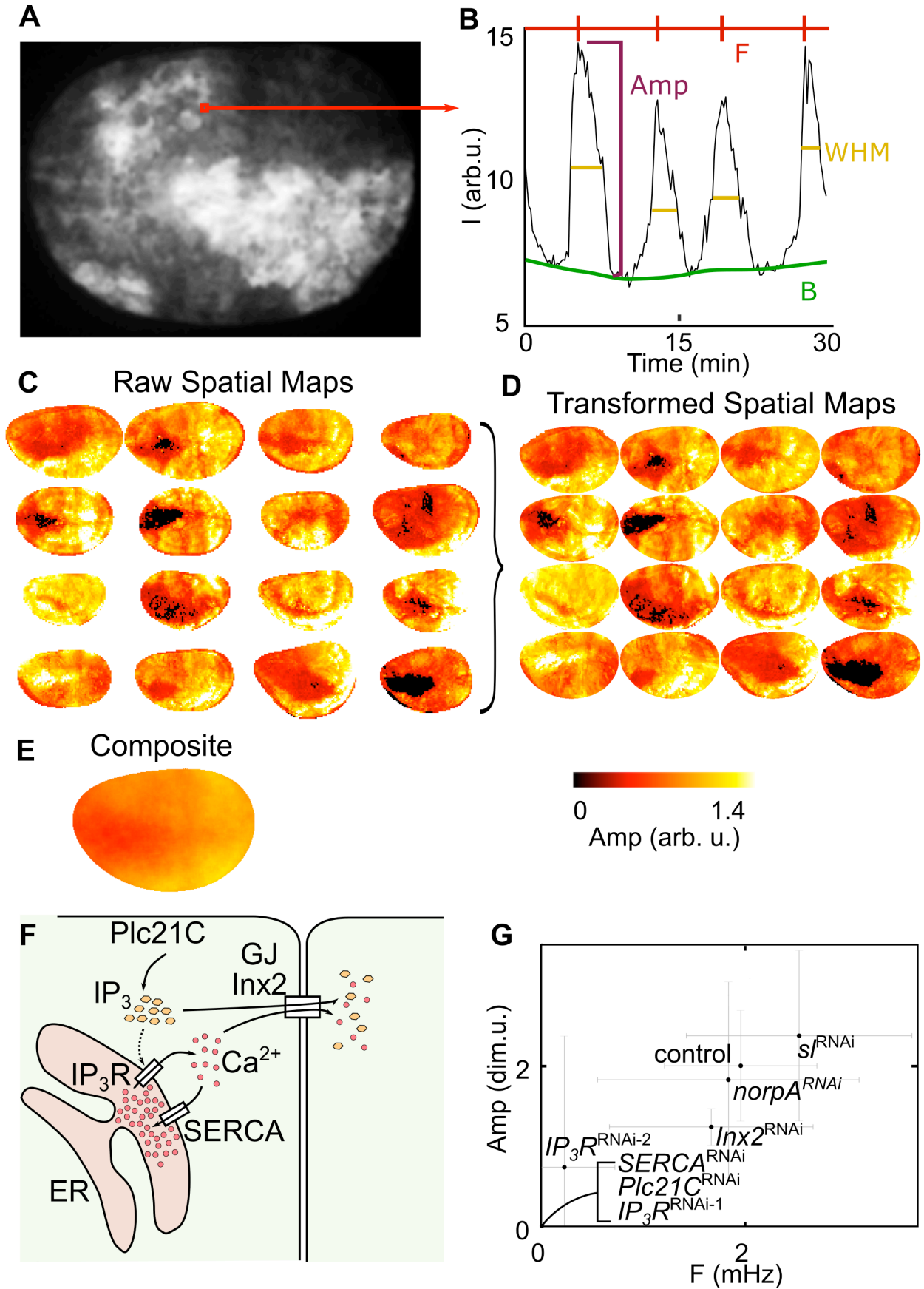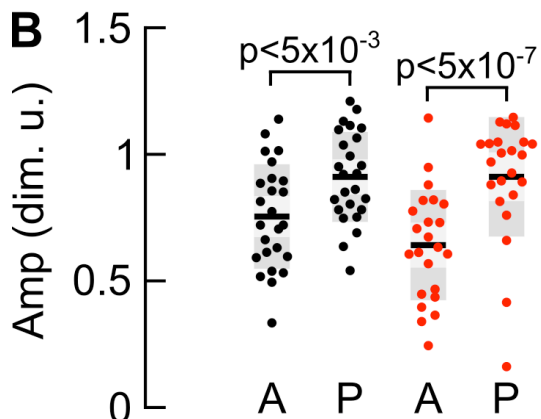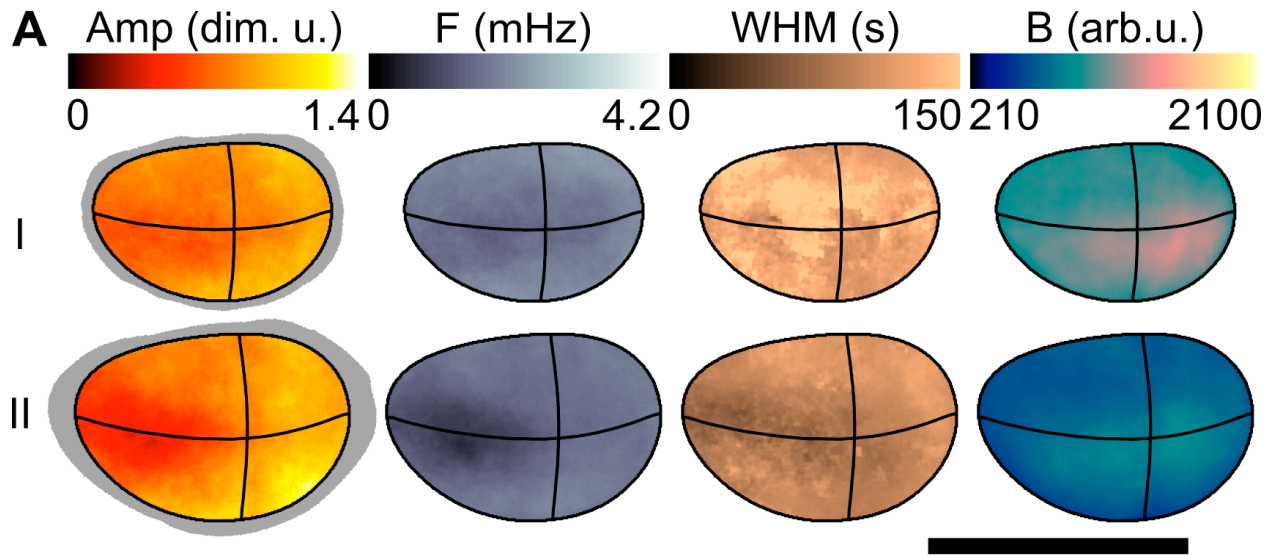
Acknowledgements

Author contributions

J.J.Z., Q.W., P.A.B., and C.N. designed and conceived the study. Q.W. and C.N. performed *ex vivo* imaging. M.L. performed *in* vivo imaging. N.A.W. performed wing imaging. P.A.B. developed image processing pipeline. J.C., P.L., and D.Z.C. developed automated methods for image segmentation, registration, and video mapping. Q.W., P.B., and J.J.Z. analyzed data and wrote the manuscript. J.J.Z supervised the study.

9

A

Wing disc

A P

Pouch (*nub*>Gal4)

B

in vivo

tape *larvae*

coverslip

C

ex vivo

filter

wing disc

glass-bottom dish

D 0 sec *in vivo* 100 sec

nub>GCaMP6f

E *ZB* No Wave

nub>GCaMP6f

F *ZB, 15% FEX* Wave

nub>GCaMP6f

G *ZB, 15% FEX* Flashes

nub>GCaMP6f,inx2^RNAi

D'

E'

F'

G'

10

A

Control

Control
n = 56

DMSO
n = 4

Canonical Activation

UAS-ci^{PKA-}
n = 18

UAS-ci
n = 7

UAS-fu
n = 14

Canonical Suppression

UAS-smo^{RNAi}
n = 11

UAS-$cos2$
n = 10

UAS-ci^{RNAi}
n = 10

Combined Canonical and Noncanonical Activation

UAS-smo^{CA}
n = 8

Noncanonical Activation

Cyclopamine
50 µM, n = 19

SQ 22536
50 µM, n = 7

B
Amp (dim. u.)

C
Amp A vs. P
P-value

*** p<1x10^{-8}
** p<0.004
** p<0.01
Deformed Low Ca^{2+} activity
** p<0.03
** p<0.006
N/S p>0.9
N/S p>0.6
N/S p>0.3
** p<0.01
*** p<3x10^{-6}
* p<0.05

D
F (mHz)

Deformed Low Ca^{2+} activity

E
F (mHz)

** p<0.005
p<0.02
N/S
*** p<4x10^{-6}
p<0.08
*** p<2x10^{-4}
N/S
* p<0.02
** p<7x10^{-3}

200 µm

13

A

Fraction

1

0.5

0

$Plc21c^{RNAi}$ control smo^{RNAi}

in vivo
waves per
20 min

■ 3+
■ 2
■ 1
■ 0

B

Hh

Ptc

UAS-smo^{RNAi}
UAS-smo^{CA}

Canonical   **Noncanonical**

Smo

UAS-ci^{RNAi}
UAS-$cos2$
UAS-fu
UAS-ci^{PKA-}
UAS-ci

Cyclopamine

Ci^{155}

HSC

Ci^R

G$_{\alpha i}$

cAMP ├── SQ 22536

? Ca^{2+}
   Freq

Higher Frequency
Multimodal effect
Lower Frequency

14

References

1. Chifflet S, et al. (2012) Early and late calcium waves during wound healing in corneal endothelial cells. *Wound Repair Regen* 20(1):28–37.

2. Justet C, Hernández JA, Torriglia A, Chifflet S (2016) Fast calcium wave inhibits excessive apoptosis during epithelial wound healing. *Cell Tissue Res*:1–14.

3. Antunes M, Pereira T, Cordeiro JV, Almeida L, Jacinto A (2013) Coordinated waves of actomyosin flow and apical cell constriction immediately after wounding. *J Cell Biol* 202(2):365–379.

4. Prevarskaya N, Skryma R, Shuba Y (2011) Calcium in tumour metastasis: new roles for known actors. *Nat Rev Cancer* 11(8):609–618.

5. Markova O, Lenne P-F (2012) Calcium signaling in developing embryos: focus on the regulation of cell shape changes and collective movements. *Semin Cell Dev Biol* 23(3):298–307.

6. Monteith GR, Davis FM, Roberts-Thomson SJ (2012) Calcium channels and pumps in cancer: changes and consequences. *J Biol Chem* 287(38):31666–31673.

7. Antunes M, Pereira T, Cordeiro JV, Almeida L, Jacinto A (2013) Coordinated waves of actomyosin flow and apical cell constriction immediately after wounding. *J Cell Biol* 202(2):365–379.

8. Deng H, Gerencser AA, Jasper H (2015) Signal integration by Ca2+ regulates intestinal stem-cell activity. *Nature* 528(7581):212–217.

9. Restrepo S, Basler K (2016) Drosophila wing imaginal discs respond to mechanical injury via slow InsP3R-mediated intercellular calcium waves. *Nat Commun* 7:12450.

10. Wallingford JB, Ewald AJ, Harland RM, Fraser SE (2001) Calcium signaling during convergent extension in Xenopus. *Curr Biol* 11(9):652–661.

11. Berridge MJ, Lipp P, Bootman MD (2000) The versatility and universality of calcium signalling. *Nat Rev Mol Cell Biol* 1(1):11–21.

12. Clapham DE (2007) Calcium Signaling. *Cell* 131(6):1047–1058.

13. Smedler E, Uhlén P (2014) Frequency decoding of calcium oscillations. *Biochim Biophys Acta BBA - Gen Subj* 1840(3):964–969.

14. Narciso C, et al. (2015) Patterning of wound-induced intercellular Ca 2+ flashes in a developing epithelium. *Phys Biol* 12(5):056005.

15. Ohno Y, Otaki JM (2015) Spontaneous long-range calcium waves in developing butterfly wings. *BMC Dev Biol* 15(1):1–13.

16. Balaji R, et al. (2017) Calcium spikes, waves and oscillations in a large, patterned epithelial tissue. *Sci Rep* 7. doi:10.1038/srep42786.

17. Narciso C, et al. (2015) Patterning of wound-induced intercellular Ca 2+ flashes in a developing epithelium. *Phys Biol* 12(5):056005.

18. Kaneuchi T, et al. (2015) Calcium waves occur as Drosophila oocytes activate. *Proc Natl Acad Sci* 112(3):791–796.

19. Kuchibhotla KV, Lattarulo CR, Hyman BT, Bacskai BJ (2009) Synchronous hyperactivity and intercellular calcium waves in astrocytes in Alzheimer mice. *Science* 323(5918):1211–1215.

20. Davis FM, et al. (2014) Induction of epithelial–mesenchymal transition (EMT) in breast cancer cells is calcium signal dependent. *Oncogene* 33(18):2307–2316.

21. Turing AM (1952) The Chemical Basis of Morphogenesis. *Philos Trans R Soc Lond Ser B* 237:37–72.

22. Wolpert L (1968) The French flag problem: a contribution to the discussion on pattern development and regulation.

23. Briscoe J, Small S (2015) Morphogen rules: design principles of gradient-mediated embryo patterning. *Development* 142(23):3996–4009.

24. Yakoby N, et al. (2008) A combinatorial code for pattern formation in Drosophila oogenesis. *Dev Cell* 15(5):725–737.

25. Ingham PW, Nakano Y, Seger C (2011) Mechanisms and functions of Hedgehog signalling across the metazoa. *Nat Rev Genet* 12(6):393–406.

26. Tabata T, Kornberg TB (1994) Hedgehog is a signaling protein with a key role in patterning Drosophila imaginal discs. *Cell* 76(1):89–102.

27. Robbins DJ, Fei DL, Riobo NA (2012) The Hedgehog Signal Transduction Network. *Sci Signal* 5(246):re6–re6.

28. Brennan D, Chen X, Cheng L, Mahoney M, Riobo NA (2012) Noncanonical Hedgehog Signaling. *Vitam Horm* 88:55–72.

29. Belgacem YH, Borodinsky LN (2011) Sonic hedgehog signaling is decoded by calcium spike activity in the developing spinal cord. *Proc Natl Acad Sci* 108(11):4482–4487.

30. Narciso CE, Contento NM, Storey TJ, Hoelzle DJ, Zartman JJ (2016) A regulated environment for micro-organs defines essential conditions for intercellular Ca2+ waves. *bioRxiv*:081869.

31. Wu Q, et al. (2017) Morphogen signalling patterns calcium waves in the Drosophila wing disc. *bioRxiv*:104745.

32. Sun XR, et al. (2013) Fast GCaMPs for improved tracking of neuronal activity. *Nat Commun* 4. doi:10.1038/ncomms3170.

33. Zartman J, Restrepo S, Basler K (2013) A high-throughput template for optimizing Drosophila organ culture with response-surface methods. *Development* 140(3):667–674.

34. Burnette M, Brito-Robinson T, Li J, Zartman J (2014) An inverse small molecule screen to design a chemically defined medium supporting long-term growth of Drosophila cell lines. *Mol Biosyst* 10(10):2713–2723.

35. Handke B, Szabad J, Lidsky PV, Hafen E, Lehner CF (2014) Towards Long Term Cultivation of Drosophila Wing Imaginal Discs In Vitro. *PLoS ONE* 9(9):e107333.

36. Fraser SE, Bryant PJ (1985) Patterns of dye coupling in the imaginal wing disk of Drosophila melanogaster. *Nature* 317(6037):533–536.

37. Hufnagel L, Teleman AA, Rouault H, Cohen SM, Shraiman BI (2007) On the mechanism of wing size determination in fly development. *Proc Natl Acad Sci* 104(10):3835–3840.

38. Bessonov N, et al. (2015) On a Model of Pattern Regeneration Based on Cell Memory. *PLOS ONE* 10(2):e0118091.

39. Basler K, Struhl G, others (1994) Compartment boundaries and the control of Drosophila limb pattern by hedgehog protein. *Nat-Lond-*:208–208.

40. Dahmann C, Oates AC, Brand M (2011) Boundary formation and maintenance in tissue development. *Nat Rev Genet* 12(1):43–55.

41. Rodriguez I, Basler K (1997) Control of compartmental affinity boundaries by Hedgehog. *Nature* 389(6651):614–618.

42. Liu C, et al. (2014) Hedgehog signaling downregulates Suppressor of Fused through the HIB/SPOP-Crn axis in Drosophila. *Cell Res* 24(5):595–609.

43. Liu Y, Cao X, Jiang J, Jia J (2007) Fused–Costal2 protein complex regulates Hedgehog-induced Smo phosphorylation and cell-surface accumulation. *Genes Dev* 21(15):1949–1963.

44. Teperino R, et al. (2012) Hedgehog Partial Agonism Drives Warburg-like Metabolism in Muscle and Brown Fat. *Cell* 151(2):414–426.

45. Alon U (2006) *An Introduction to Systems Biology: Design Principles of Biological Circuits* (CRC Press).

46. Hart Y, Antebi YE, Mayo AE, Friedman N, Alon U (2012) Design principles of cell circuits with paradoxical components. *Proc Natl Acad Sci* 109(21):8346–8351.

47. Hart Y, Alon U (2013) The Utility of Paradoxical Components in Biological Circuits. *Mol Cell* 49(2):213–221.

48. Gurdziel K, et al. (2015) Identification and Validation of Novel Hedgehog-Responsive Enhancers Predicted by Computational Analysis of Ci/Gli Binding Site Density. *PLOS ONE* 10(12):e0145225.

49. Corrigall D, Walther RF, Rodriguez L, Fichelson P, Pichaud F (2007) Hedgehog Signaling Is a Principal Inducer of Myosin-II-Driven Cell Ingression in Drosophila Epithelia. *Dev Cell* 13(5):730–742.

50. Czerniak ND, Dierkes K, D'Angelo A, Colombelli J, Solon J (2016) Patterned Contractile Forces Promote Epidermal Spreading and Regulate Segment Positioning during Drosophila Head Involution. *Curr Biol* 26(14):1895–1901.

51. Lechner H, Josten F, Fuss B, Bauer R, Hoch M (2007) Cross regulation of intercellular gap junction communication and paracrine signaling pathways during organogenesis in Drosophila. *Dev Biol* 310(1):23–34.

52. Martín FA, Morata G (2006) Compartments and the control of growth in the Drosophila wing imaginal disc. *Dev Camb Engl* 133(22):4421–4426.

53. Alon U (2007) Network motifs: theory and experimental approaches. *Nat Rev Genet* 8(6):450–461.

54. Yeger-Lotem E, et al. (2004) Network motifs in integrated cellular networks of transcription–regulation and protein–protein interaction. *Proc Natl Acad Sci U S A* 101(16):5934–5939.

55. Hart Y, Alon U (2013) The Utility of Paradoxical Components in Biological Circuits. *Mol Cell* 49(2):213–221.

56. Bryant PJ, Fraser SE (1988) Wound healing, cell communication, and DNA synthesis during imaginal disc regeneration in Drosophila. *Dev Biol* 127(1):197–208.

57. Bassett JJ, Monteith GR (2017) Genetically Encoded Calcium Indicators as Probes to Assess the Role of Calcium Channels in Disease and for High-Throughput Drug Discovery. *Adv Pharmacol*. Available at: http://www.sciencedirect.com/science/article/pii/S1054358917300017 [Accessed March 27, 2017].

58. Schindelin J, et al. (2012) Fiji: an open-source platform for biological-image analysis. *Nat Methods* 9(7):676–682.

59. Schaffter T (2014) From genes to organisms: Bioinformatics system models and software. Dissertation (ÉCOLE POLYTECHNIQUE FÉDÉRALE DE LAUSANNE, Laboratory of Intelligent Systems, EPFL, Switzerland).

Fig. 1. Intercellular Ca^{2+} waves (ICWs) in *Drosophila* wing discs. (A) Cartoon of wing disc model system. The wing disc is subdivided into lineage-restricted anterior-posterior compartments. Gene expression in the pouch can be modulated with Gal4/UAS system using the nubbin-GAL4 driver. (B) Wing disc imaged in the in vivo imaging setup. (C) Wing disc ex vivo imaging setup. (D) In vivo confocal imaging of GCaMP6f during an ICW (E-G), Ex vivo confocal imaging of GCaMP6f. (D'-G'), Isosurfaces of GCaMP6f fluorescence over time: D', in vivo, E', in ZB media; F', in ZB media with 15% fly extract; G', wing discs with reduced gap junction communication through knockdown of Inx2 in ZB media with 15% fly extract.

Fig. 2. Image analysis and mechanisms of ICW propagation. (A) Illustration of region-of-interest (ROI) based extraction of Ca^{2+} traces from the wing disc pouch. (B) Extraction of amplitudes (Amp), frequency (F), width at half max (WHM) and amplitude (Amp) from Ca^{2+} trace for individual regions-of-interest (ROI). (C) Spatial maps of Amp in multiple pouches. (D) Spatial maps transformed onto "average" pouch shape. (E) Median projection of 54 transformed spatial maps of Amp. (F) Schematic of ICW mechanism in the wing disc as verified by this study and previous work (9, 14, 30). (G) Average frequency and amplitude of ICWs in different genetic perturbation backgrounds. Error bars represent standard deviation. ICWs require Plc21C. IP$_3$: inositol-1,4,5-trisphosphate; ER: endoplasmic reticulum; SERCA: sarco/endoplasmic reticulum Ca^{2+} ATPase; GJ: gap junction.

Fig. 3. ICWs are spatiotemporally patterned during development. Pouches were grouped by pouch size for comparison of "younger" discs to "older" discs. Calcium signaling in nub-GAL4; UAS-GCaMP6f pouches followed one of two patterns: small pouches with high WHM and basal intensity, and larger pouches with a higher Amp in the P compartment. A) Composite spatial maps of the median ICW summary statistics. Grey shaded region represents areal extent of 95% of pouches in each of the two groups. B) Average amplitude (Amp, dim. u.) for each compartment was greater in the P compartment for the class of larger pouch sizes by student t-test, C) frequency, F (mHz) did not change over development, D) width at half max, WHM (s) decreased slightly over development (for exponential fit, adjusted R^2=0.15, $p<3\times10^{-3}$ by F-test), E) and basal intensity, B (arb. u.) decreased over development (for exponential fit, adjusted R^2=0.77, $p<1\times10^{-17}$ by F-test). Grey shaded area is the 95% confidence interval of predicted data. Scale bar represents 200 μm.

Fig. 4. Hedgehog signaling regulates ICW dynamics. (A) Genetic and drug perturbations and their corresponding sample size (n). (B) Composite spatial maps for ICW amplitudes. Grey shaded region represents areal extent of 95% of pouches. (C) P-value of amplitudes between A and P compartments. (D) Composite spatial maps of ICW frequencies. Scale bar represents 200 μm. (E) Distribution of frequencies within ROIs within discs. In (E), red line error bars indicate average value with standard deviation. Genetic perturbations are compared to "control" (nub-GAL4; UAS-GCaMP6f), and pharmacological perturbations compared to "DMSO" (nub-GAL4; UAS-GCaMP6f treated with 0.1% DMSO for 1 hour). Dotted grey line indicates baseline frequency. * $p<0.05$, ** $p<0.01$, and *** $p<0.001$ by Student's t-test. Scale bar: 200 μm.

Fig. 5. Hedgehog signaling regulates ICW frequency *in vivo*. (*A*) *in vivo* ICW frequency in immobilized larvae. n = 11, 72, and 28. *In vivo* results of ICWs match those of *ex vivo* results, where *Plc21C* [RNAi] abolished ICWs and *smo*[RNAi] increases ICW frequency. (*B*) Proposed mechanism for regulation of ICW frequencies by Hh signaling.

Supporting Information

Fig. S1. Signal extraction from wing discs. (*A*) t-slice projection of time-lapse video. (*B*) Manual mask around pouch, and grid of square regions of interest (ROIs). (*C*) Individual ROI is averaged over space to obtain a one-dimensional (1D) intensity profile. (*D*) Raw intensity profile. (*E*) Normalized intensity profile with amplitudes and widths at half max (WHM) marked. (*F*) Number of square ROIs extracted from each pouch. (*G*) Distribution of analysed duration for each pouch, corresponding to durations when minimal movement occurred during live imaging.

Fig. S2. Optimization of image analysis parameters. (*A*) Pareto optimization chart for final solution. b-d, Comparison of automatically-extracted values and manually measured values for (*B*) frequency, (*C*) amplitude, and (*D*) time between peaks.
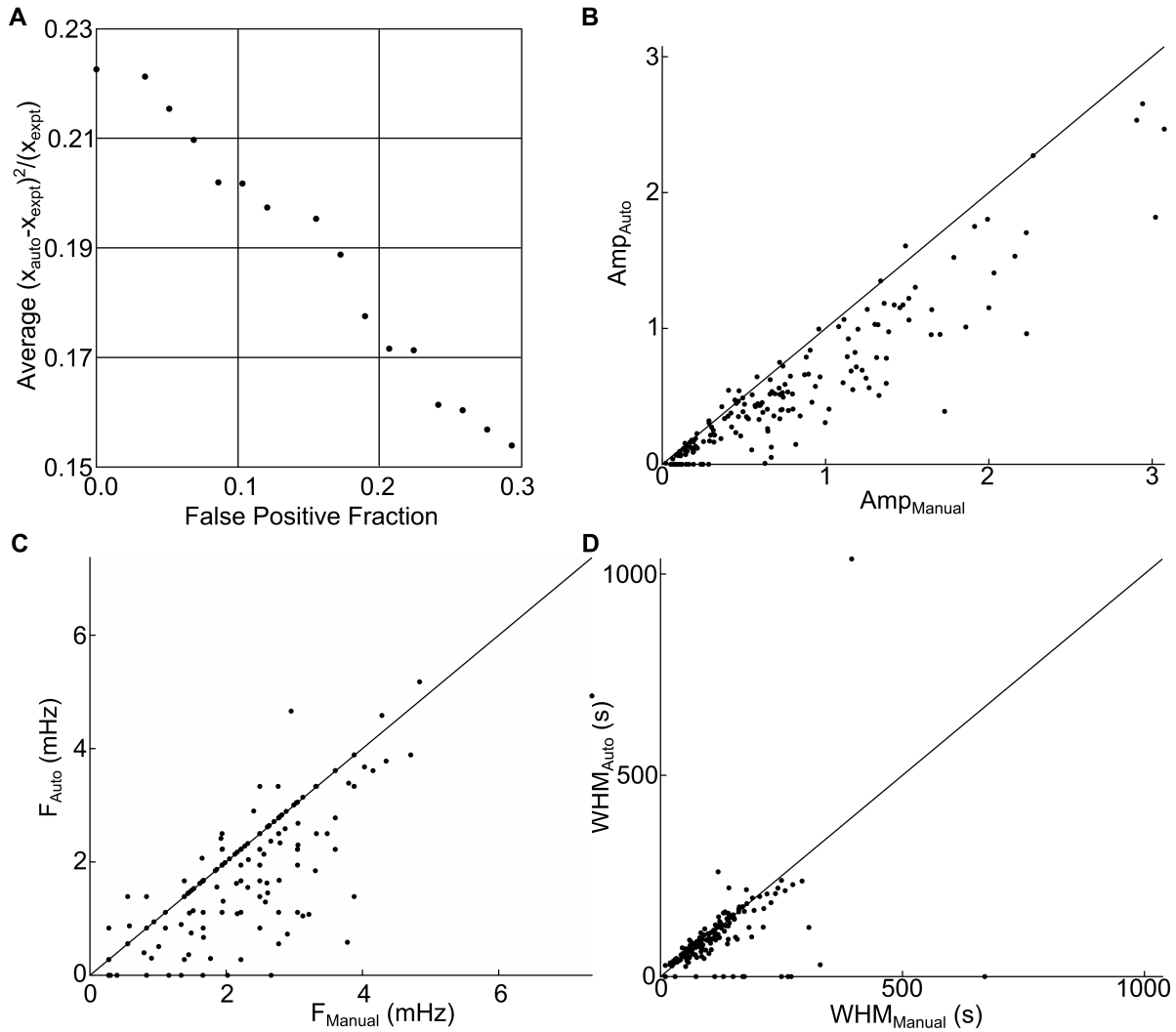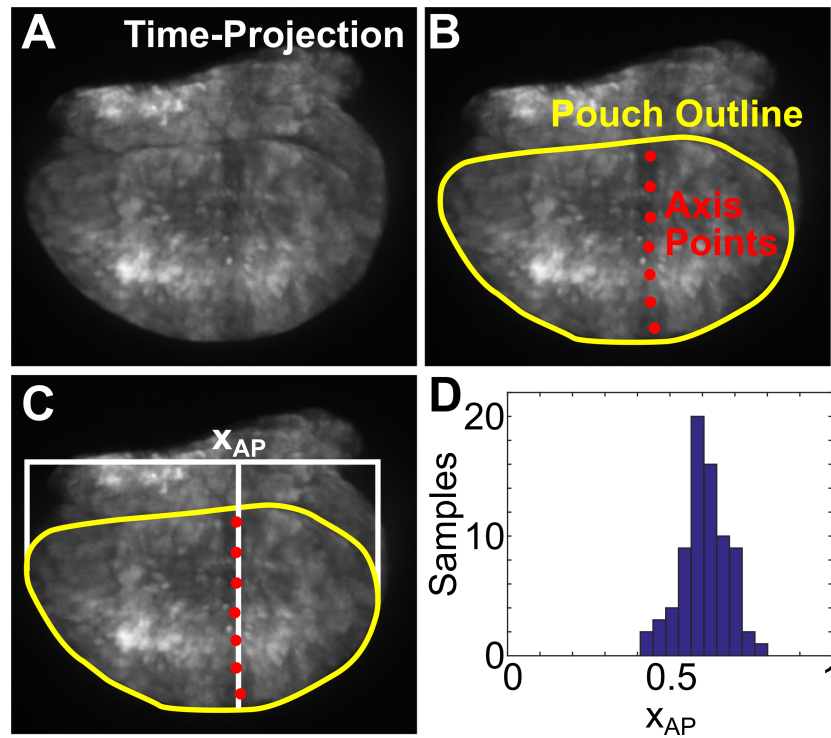
Fig. S3. Manual segmentation of the wing disc pouch. (*A*) Max time-projection of control time-lapse oriented as described in Fig. S1*A-B*. (*B*) Pouch segmented by selecting points along the pouch boundary, which has an edge of lower intensity. Points selected along A/P axis, which is a region of lower intensity. (*C*) Vertical line is fit to selected points, with position x_{AP}. For analysis, anterior (A) compartment is to the left of x_{AP}, and posterior (P) compartment is to the right of x_{AP}. (D) Distribution of x_{AP} for control pouches. $x_{AP} = 0.61 \pm 0.07$, therefore the P compartment is slightly smaller than the A compartment (1).

Wildtype yw

nub>GCaMP6f/yw (control)

nub>GCaMP6f,plc21c^{RNAi}

nub>GCaMP6f,sl^{RNAi}

nub>GCaMP6f,norpA^{RNAi}

nub>GCaMP6f,ip3r^{RNAi}

nub>GCaMP6f,serca^{RNAi}

nub>GCaMP6f,ryr^{RNAi}

nub>GCaMP6f,stim^{RNAi}

nub>GCaMP6f,orai^{RNAi}

nub>GCaMP6f,pmca^{RNAi}

nub>GCaMP6f,inx2^{RNAi}

nub>GCaMP6f,smo^{RNAi}

nub>GCaMP6f,Smo-CA

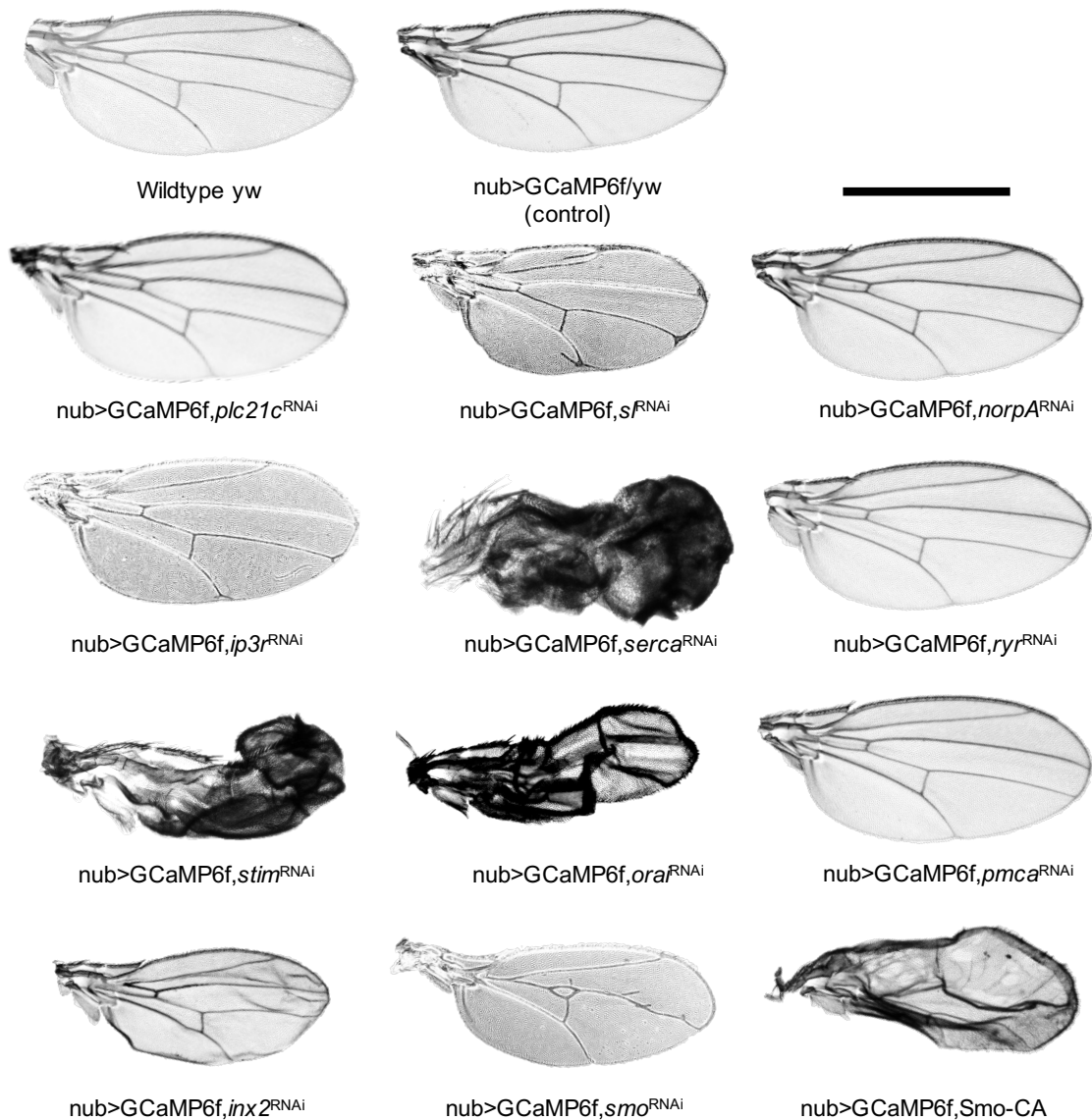**Fig. S4.** Example wing phenotypes from Ca^{2+} and Hh perturbation lines. Shown here are representative images from each genetic condition. sl^{RNAi} led to smaller wings, and the end of the veins bifurcated. norpA^{RNAi} and ryr^{RNAi} did not change wing morphology. ip3r^{RNAi} resulted in the bifurcation of L4 & L5 veins. serca^{RNAi}, stim^{RNAi}, orai^{RNAi}, Smo-CA led to underdeveloped wings. pmca^{RNAi} led to a slightly bigger wing. inx2^{RNAi} resulted in a much smaller wing than control, and the wing is wrinkled. smo^{RNAi} led to the disappearance of the area between L3 & L4 veins, and the two merge. Control was generated from crossing the tester line (nub>GCaMP6/CyO) to yw. The genetic perturbation lines (the rest of the wings) were generated by crossing the tester line to UAS-Plc21C^{RNAi} (BL# 33719), sl^{RNAi} (BL# 32906), norpA^{RNAi} (BL# 31113), Ip3r^{RNAi} (BL# 25937), serca^{RNAi} (BL# 44581), ryr^{RNAi} (BL# 31540), stim^{RNAi} (BL# 27263), orai^{RNAi} (BL# 53333), pmca^{RNAi} (BL# 31572), inx2^{RNAi} (BL# 29306), smo^{RNAi} (BL# 43134), Smo-CA

(BL# 44621), respectively. Vein bifurcation: arrow; vein merging: arrowhead. Scale bar: 1 mm.
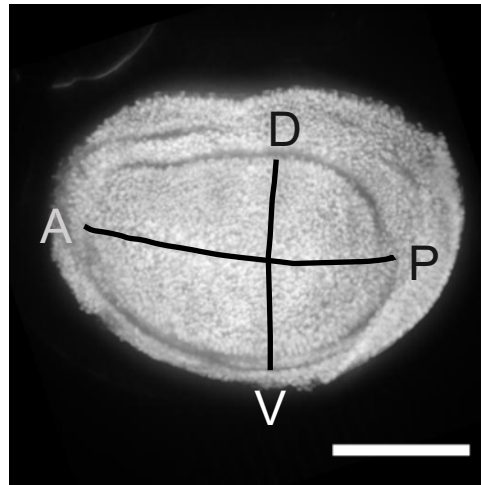
Fig. S5. *nubbin-Gal4* driven expression is uniform in the wing disc pouch. *nub-Gal4>UAS-RFP* is expressed in the pouch. The intensity of RFP is uniform throughout the disc, suggesting uniform expression of GCaMP6 calcium sensor. A: anterior; P: posterior; D: dorsal; V: ventral. Scale bar: 50 μm.
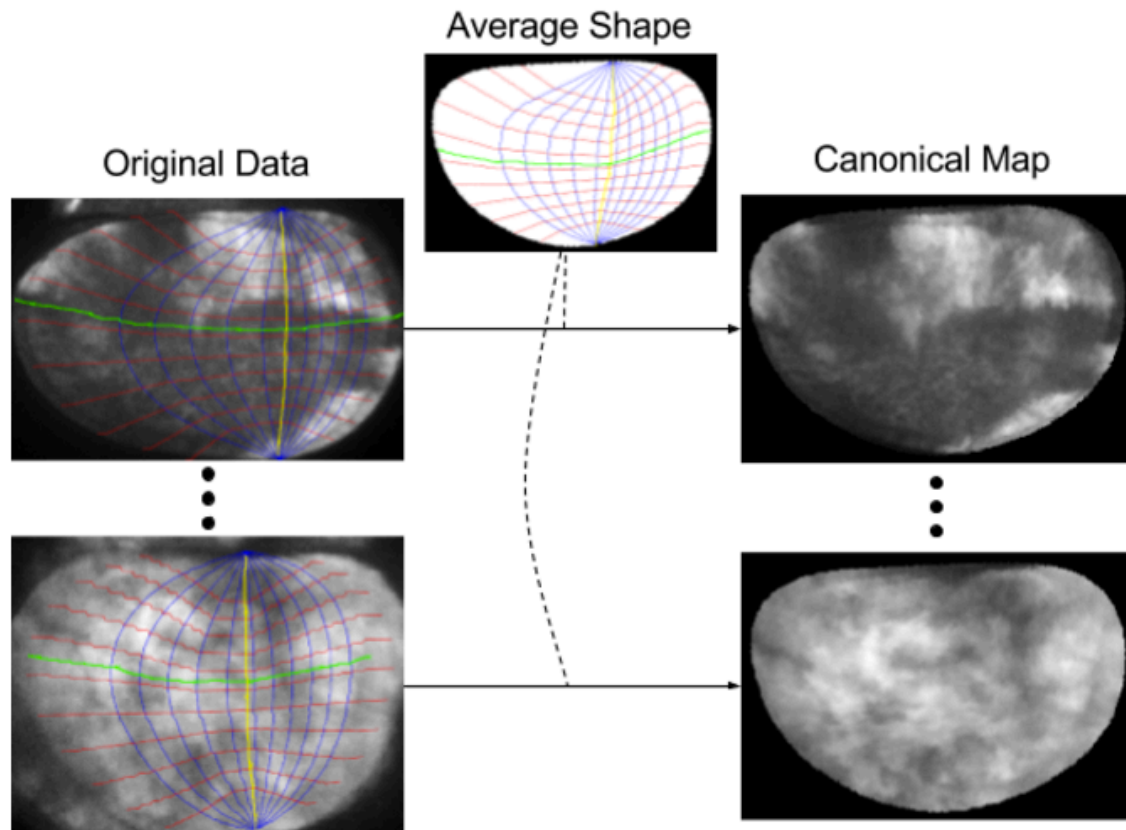
Fig. S6. Illustrating the computation of canonical pouch representation. A pouch coordinate system is defined along the A/P axis (the green curve) and the D/V axis (the yellow curve), similar to the latitude (cf. red curves) and longitude (cf. blue curves) of the geographic coordinate system, and is constructed for each pouch. A mapping from the pouch coordinates in an input image to the corresponding pouch coordinates of the average shape transforms the original data to a canonical map.

Table S1 | This table relates to Fig. 3*B-E.*

Size Bin	Pouch Size μm^2 x 10^3	n	N	Student's paired t test (A vs P)				Wilcoxon rank sum test (A vs P)			
				Amp	F	D	B	Amp	F	D	B
I	14-17	29	19	2.0E-3	0.31	0.50	0.12	3.9E-3	0.36	0.25	4.5E-3
II	17-20	27	15	1.1E-6	3.0E-2	0.14	0.07	4.6E-5	1.27E-2	0.14	0.11

N = number of imaging sessions, n = number of samples

29

Table S2 | Wing phenotypes

Gene	BL#	Genotype (UAS-line)	Progeny Wing Phenotype
UAS-Plc21C^{RNAi}	33719	y[1] sc[*] v[1]; P{y[+t7.7] v[+t1.8]=TRiP.HMS00600}attP2	The tip of L2 vein bends slightly upward.
UAS-*sl*^{RNAi}	32906	y[1] sc[*] v[1]; P{y[+t7.7] v[+t1.8]=TRiP.HMS00695}attP2	Wings are smaller.
UAS-norpA^{RNAi}	31113	y[1] v[1]; P{y[+t7.7] v[+t1.8]=TRiP.JF01585}attP2	The tip of L2 vein bends slightly upward.
UAS-IP3R^{RNAi}	25937	y[1] v[1]; P{y[+t7.7] v[+t1.8]=TRiP.JF01957}attP2	The tip of L2 vein bends slightly upward.
	51795	y[1] sc[*] v[1]; P{y[+t7.7 v[+t1.8]=TRiP.HMC03351}attP40	The tip of L2 vein bends slightly upward.
UAS-SERCA^{RNAi}	44581	y[1] v[1]; P{y[+t7.7] v[+t1.8]=TRiP.JF01948}attP2	Wing did not form properly.
UAS-*Ryr*^{RNAi}	31540	y[1] v[1]; P{y[+t7.7] v[+t1.8]=TRiP.JF01100}attP2	Normal
UAS-*Stim*^{RNAi}	27263	y[1] v[1]; P{y[+t7.7] v[+t1.8]=TRiP.JF02567}attP2	Crumpled wings.
UAS-*Orai*^{RNAi}	53333	y[1] sc[*] v[1]; P{y[+t7.7] v[+t1.8]=TRiP.HMC03562}attP40	Crumpled wings.
UAS-*Inx2*^{RNAi}	29306	y[1] v[1]; P{y[+t7.7] v[+t1.8]=TRiP.JF02446}attP2	Wings are smaller.
UAS-*Smo*^{RNAi}	43134	y[1] v[1]; P{y[+t7.7] v[+t1.8]=TRiP.GL01472}attP2	Merging of L3 & L4. The development between L3 & L4 is disrupted.
	27037	y[1] v[1]; P{y[+t7.7 v[+t1.8]=TRiP.JF02363}attP2	Merging of L3 & L4. The development between L3 & L4 is disrupted (Less strong than BL#43134).
	53348	y[1] sc[*] v[1]; P{y[+t7.7 v[+t1.8]=TRiP.HMC03577}attP40	Merging of L3 & L4. The development between L3 & L4 is disrupted (Less strong than BL#43134).
UAS-Smo^{CA}	44621	y[1] w[*]; P{w[+mC]=UAS-FLAG-smo.act}2	Wing did not form properly.
	44620	w[*]; P{w[+mC]=UAS-smo.H}3	Wing did not form properly.
UAS-*Fu*^{RNAi}	31043	y[1] v[1]; P{y[+t7.7] v[+t1.8]=TRiP.JF01490}attP2	Merging of L3 & L4 veins at the beginning. No anterior cross vein. Bifurcation at the end of L3 & L4 veins
	41588	y[1] v[1]; P{y[+t7.7] v[+t1.8]=TRiP.GL00705}attP40	No phenotype
UAS-*SuFu*^{RNAi}	28559	y[1] v[1]; P{y[+t7.7] v[+t1.8]=TRiP.HM05045}attP2	No phenotype
UAS-*Ci*^{RNAi}	31236	y[1] v[1]; P{y[+t7.7] v[+t1.8]=TRiP.JF01744}attP2	Merging of V3 & V4 at the beginning
	31320	y[1] v[1]; P{y[+t7.7] v[+t1.8]=TRiP.JF01810}attP2	Merging of V3 & V4 at the beginning (Stronger phenotype)

Table S3 | This table relates to Fig. 4.

Condition	n	N	Student's unpaired t test vs control		Wilcoxon signed rank test vs Control		Student's paired t test (A vs P)		Wilcoxon rank sum test (A vs P)	
			Amp	F	Amp	F	Amp	F	Amp	F
control	56	26	1	1	1	1	2E-8	2E-2	5E-7	2E-2
DMSO (0.1%)	4	1	1	1	1	1	7E-3	0.11	0.13	0.13
no FEX	2	1	6E-6	4E-3	2E-2	2E-2	N/A	N/A	1	1
BL#25937 IP3R RNAi	4	1	2E-9	8E-5	1E-3	1E-3	N/A	N/A	1	1
BL#51795 IP3R RNAi	5	1	7E-5	1E-4	3E-2	1E-3	0.37	0.37	1	1
BL#372 PLCgamma RNAi	3	1	0.47	0.43	0.57	0.52	0.22	0.86	0.50	1
BL#33719 PLC21C RNAi	5	1	9E-11	1E-5	3E-4	3E-4	N/A	N/A	1	1
BL#31113 norpA RNAi	4	2	0.25	0.64	9E-1	0.96	0.64	0.85	1	1
BL#44581 Serca RNAi	10	2	1E-16	5E-9	9E-7	9E-7	N/A	N/A	1	1
BL#27263 Stim RNAi	3	1	5E-3	0.64	8E-3	0.55	0.15	0.42	0.25	1
BL#53333 Orai RNAi	5	1	2E-2	0.44	7E-3	0.37	0.83	7E-2	0.63	0.25
BL#29306 Inx2 RNAi	5	1	2E-2	0.37	6E-3	0.47	0.21	1.00	6E-2	1
BL#44621 smo CA	8	4	0.14	2E-3	4E-2	7E-2	9E-3	1E-2	8E-3	2E-2
BL#55072 UAS fu	14	3	4E-2	0.96	5E-2	0.92	5E-3	3E-2	4E-4	2E-2
BL#32570 UAS ci	3	1	6E-2	2E-2	7E-2	2E-2	0.18	0.27	0.25	0.50
BL#32571 UAS ci PKA-	18	5	2E-2	5E-3	1E-2	4E-3	1E-2	0.11	2E-2	0.21
BL#43134 smo RNAi	2	1	0.94	0.45	0.92	0.46	0.76	0.96	1	1
BL#27037 smo RNAi	6	3	7E-3	3E-6	2E-3	3E-4	0.95	0.39	0.84	0.44
BL#53348 smo RNAi	3	1	0.26	3E-2	0.13	6E-2	0.96	0.18	1	0.50
BL#55041 UAS cos2	10	5	2E-2	8E-2	0.14	7E-2	0.66	0.22	6E-1	0.38
BL#31236 ci RNAi	7	2	3E-3	2E-4	3E-3	3E-3	2E-2	0.60	3E-2	0.63
BL#31320 ci RNAi	3	1	1E-3	0.73	7E-3	0.70	0.21	0.42	0.50	1
Cyclopamine (100 uM)	19	6	3E-3	2E-2	1E-2	3E-2	3E-6	0.92	3E-4	0.88
SQ 22536 (50 uM)	7	2	3E-2	6E-3	4E-2	6E-3	6E-2	0.90	8E-2	1

n represents number of pouches analysed. N represents number of imaging sessions analysed. Significance tests were performed to determine whether median values were different from control values, and to determine whether A compartment values were different from P compartment values. N/A: there is no wave in those conditions, therefore, no value for the t-test.

Table S4 | SI Movies

SI Movie #	Description
1	*in vivo* waves in control tester line background (w1118; nubbin-GAL4, UAS-GCaMP6f/CyO)
2	Wing disc from tester line cultured in ZB media
3	Wing disc from tester line cultured in ZB media + FEX
4	w1118; nub-G4>UAS-GCaMP6f, UAS-*Plc21C*[RNAi] BL#33719
5	w1118; nub-G4>UAS-GCaMP6f, UAS-*sl*[RNAi] BL#32906
6	w1118; nub-G4>UAS-GCaMP6f, UAS-*norpA*[RNAi] BL#31113
7	w1118; nub-G4>UAS-GCaMP6f, UAS-*IP3R*[RNAi] BL#25937
8	w1118; nub-G4>UAS-GCaMP6f, UAS-*SERCA*[RNAi] BL#44581
9	w1118; nub-G4>UAS-GCaMP6f, UAS-*Inx2*[RNAi] BL#29306
10	w1118; nub-G4>UAS-GCaMP6f, UAS-*Stim*[RNAi] BL#27263
11	w1118; nub-G4>UAS-GCaMP6f, UAS-*Orai*[RNAi] BL#53333
12	w1118; nub-G4>UAS-GCaMP6f, UAS-*PMCA*[RNAi] BL#31572
13	w1118; nub-G4>UAS-GCaMP6f, UAS-Fu BL#55072
14	w1118; nub-G4>UAS-GCaMP6f, UAS-Ci BL#32570
15	w1118; nub-G4>UAS-GCaMP6f, UAS-Ci[PKA-] BL#32571
16	w1118; nub-G4>UAS-GCaMP6f, UAS-*smo*[RNAi] BL#27037
17	w1118; nub-G4>UAS-GCaMP6f, UAS-Cos2 BL#55041
18	w1118; nub-G4>UAS-GCaMP6f, UAS-*ci*[RNAi] BL#31320
19	In vivo, w1118; nub-G4>UAS-GCaMP6f, UAS-*smo*[RNAi] BL#27037
20	w1118; nub-G4>UAS-GCaMP6f, UAS-Smo[CA] BL#44621
21	Wing disc from tester line cultured in ZB media + FEX + DMSO 0.1%
22	Wing disc from tester line cultured in ZB media + FEX + Vismodegib 1 µM
23	Wing disc from tester line cultured in ZB media + FEX + Cyclopamine 100 µM
24	Wing disc from tester line cultured in ZB media + FEX + SQ 22536 50 µM

Table S5 | Parameters of feature extraction pipeline

Parameter	Optimized Value	Meaning
Amp_{min}	0.29	Minimum peak amplitude
WHM_{min}	23 s	Minimum duration of peak
Refractory Period	10 s	Minimum time between peaks
σ_{min}	8 s	Parameter for high-frequency Gaussian filter for removing noise
σ_{max}	1100 s	Parameter for low-frequency Gaussian filter for adapting to changes in basal level

Extended Data References

1. Martín FA, Morata G (2006) Compartments and the control of growth in the Drosophila wing imaginal disc. *Dev Camb Engl* 133(22):4421–4426.